MATERIALS SCIENCE

Redefining the limits of actuating fibers via mesophase control: From contraction to elongation

Jin-Hyeong Lee[1], Seungjoon Oh[1], In-sun Jeong[2], Yoo Jin Lee[3], Min Chan Kim[1], Jong S. Park[1], Kyu Hyun[1], Taylor H. Ware[3,4], Suk-kyun Ahn[1,2]*

The development of fibrous actuators with diverse actuation modes is expected to accelerate progress in active textiles, robotics, wearable electronics, and haptics. Despite the advances in responsive polymer-based actuating fibers, the available actuation modes are limited by the exclusive reliance of current technologies on thermotropic contraction along the fiber axis. To address this gap, the present study describes a reversible and spontaneous thermotropic elongation (~30%) in liquid crystal elastomer fibers produced via ultraviolet-assisted melt spinning. This elongation arises from the orthogonal alignment of smectogenic mesogens relative to the fiber axis, which contrasts the parallel alignment typically observed in nematic liquid crystal elastomer fibers and is achieved through mesophase control during extrusion. The fibers exhibiting thermotropic elongation enable active textiles increase pore size in response to temperature increase. The integration of contracting and elongating fibers within a single textile enables spatially distinct actuation, paving the way for innovations in smart clothing and fiber/textile actuators.

INTRODUCTION

High-temperature drying often results in undesirable permanent garment shrinkage because of fiber orientation during manufacturing (*1*, *2*). However, the entropy-driven thermotropic shrinkage in polymeric chains can be harnessed to achieve diverse in- and out-of-plane actuation modes and thus enable the creation of smart textiles, artificial muscles, and soft robots (*2*, *3*). Among various classes of actuating polymers, liquid crystal elastomers (LCEs), which combine the elasticity of elastomers with the anisotropy of liquid crystals (LCs), are particularly appealing for realizing programmable and reversible actuation in response to external stimuli in the solid state (*4*–*7*). In particular, one-dimensional (1D) LCE fibers have drawn considerable attention, as they resemble biological muscles in structural design, function, and performance, provide fast responses, and are easily processed into functional yarns or textiles with complex structures through weaving, knitting, and braiding (*8*–*10*).

LCE fibers can be produced by pulling (*11*–*13*), templating (*14*–*16*), microfluidic process (*17*, *18*), melt and solution spinning (*19*–*26*), and electrospinning (*27*–*29*). Aligned LCE fibers were first produced in 2003 by pulling a side-chain LCE melt using tweezers (*11*). Subsequently, the Terentjev group (*19*) introduced a melt extrusion method for producing uniform and considerably longer thermoplastic LCE fibers in 2006. More recently, scalable approaches have been developed by combining melt or solution spinning processes with two-step cross-linking schemes (*30*, *31*), enabling the larger-scale production of robust LCE fibers (*20*, *21*). Building on this approach using commercially available materials, various LCE fibers for artificial muscles (*32*), soft robots (*33*, *34*), automatic garments (*35*), mechanochromic textiles (*36*), and other applications have been prepared (*37*). Despite their potential for commercial applications, current LCE fiber technologies exclusively rely on thermotropic contraction along the fiber axis. In general, spontaneous and substantial thermotropic fiber elongation (>20%) upon heating, with recovery to the original length upon cooling, are difficult to realize because of the inherent polymer orientation along the fiber axis, unless using extremely twisted or coiled structures (*2*, *38*). Nonetheless, garments crafted from fibers exhibiting such thermotropic elongation would be highly valuable for temperature regulation, as their tightness or pore size can be decreased or increased with increasing temperature, respectively, offering enhanced comfort and breathability (*39*, *40*).

Realizing LCE fibers exhibiting considerable elongation upon heating requires the mesogens and polymer chains to be oriented perpendicularly to the fiber axis. A templating approach allows for the control of mesogen orientation in LCE fibers through surface-enforced alignment; however, it is limited in mass production (*14*). Recently, the Largerwall group produced hollow nematic fibers through microfluidic wet spinning, where the mesogens are oriented perpendicular to the tube axis after solvent removal, enabling thermotropic elongation (*18*). However, the resulting fibers exhibit considerably weak mechanical strength (several kilopascals), limiting their broader applications.

To address the aforementioned gap, we herein report mechanically robust smectic LCE fibers produced via melt spinning, which undergo a spontaneous elongation (>30%) upon heating and returning to the initial length upon cooling. Unlike conventional fibers and most reported LCE fibers with alignment along the fiber axis, the elongating smectic LCE fibers in this study feature mesogen alignment perpendicular to the fiber axis. The orientation and resulting actuation direction are determined by the LC phase during melt extrusion, with the extrusion of nematic and isotropic melts affording contracting fibers and that of the smectic melt affording elongating fibers.

[1]School of Chemical Engineering, Pusan National University, Busan, Republic of Korea. [2]Department of Polymer Science and Engineering, Pusan National University, Busan, Republic of Korea. [3]Department of Biomedical Engineering, Texas A&M University, College Station, TX, USA. [4]Department of Materials Science and Engineering, Texas A&M University, College Station, TX, USA.
*Corresponding author. Email: skahn@pusan.ac.kr

RESULTS

Molecular alignment and actuation of LCE fibers

Conventional LCE fibers are produced through melt spinning from nematic oligomers as precursors (*8*, *9*, *21*). Upon extrusion through

a nozzle, the directors in main-chain nematic oligomers are aligned in the shear flow direction (Fig. 1A). In contrast, molecular orientation orthogonal to the flow direction can be achieved when smectic oligomers are extruded (Fig. 1B). Under shear flow, smectic melts can undergo molecular orientation, with the fluidic smectic layers and mesogens within them aligning parallel and perpendicular to the flow direction, respectively, as observed for low–molecular weight smectic LCs and polymeric smectics (*41*–*45*). This orientation, especially in polymeric smectic melts, arises because the sliding between mesogens within the layer is difficult while that between the domain boundaries of chain-folded smectic lamellae is relatively easy (*43*). Taking advantage of the molecular orientation of the smectic phase, we produced uniformly aligned LCE fibers with a length of 15 m and a diameter of 380 to 480 μm through melt

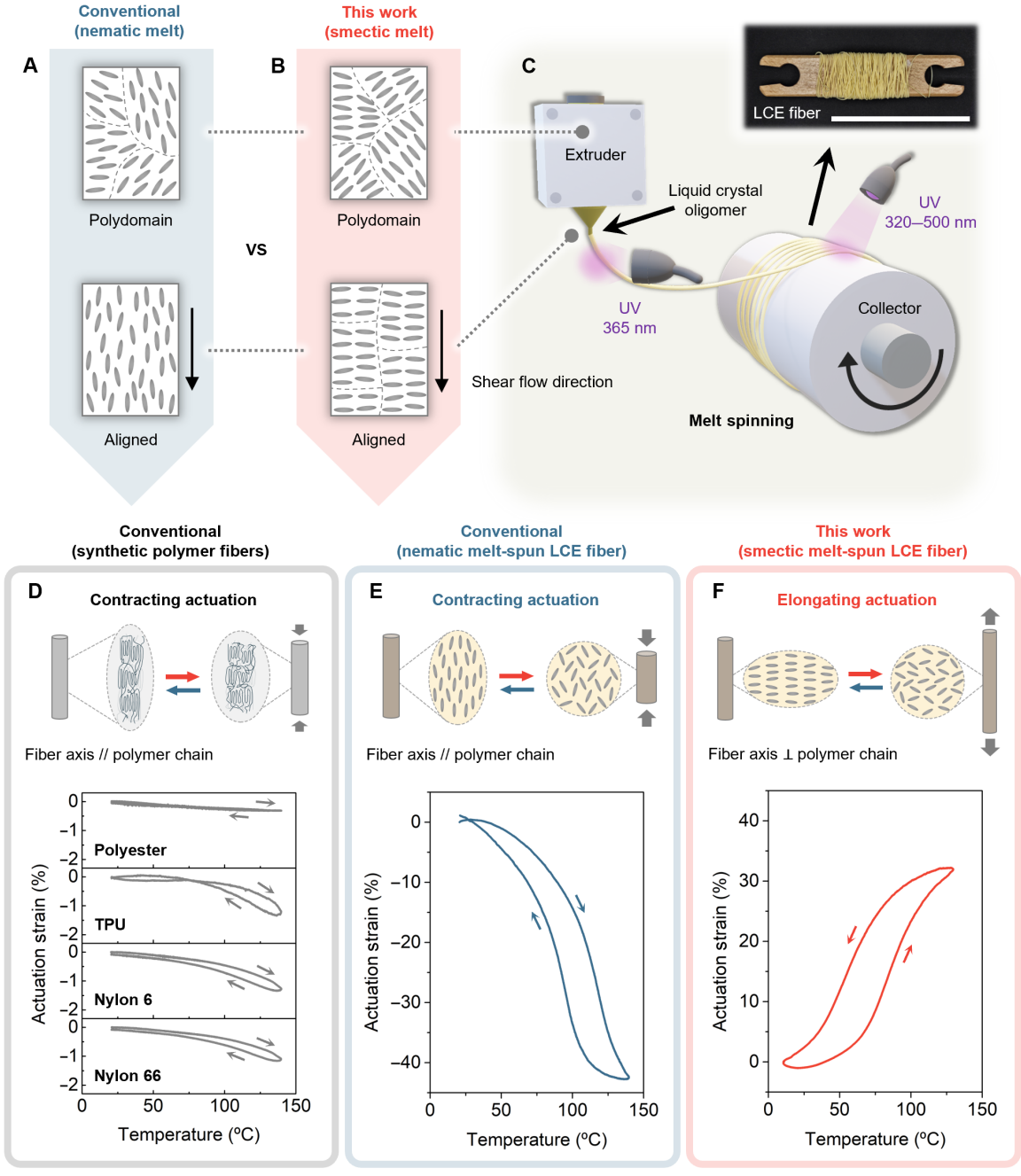

Fig. 1. Production, alignment, and actuation of LCE fibers. (**A** and **B**) Molecular alignment of (A) nematic and (B) smectic oligomers during extrusion. (**C**) Production of LCE fibers through UV-assisted melt spinning. A photograph of the smectic fiber product is shown in the inset. Scale bar, 10 cm. (**D** to **F**) Schematic of the molecular structure and thermal actuation measured by dynamic mechanical analysis of (D) commercial monofilament fibers, (E) nematic fiber, and (F) smectic fiber during heating and cooling. Actuation strain (%) $= [L(T) - L_0] / L_0 \times 100$ (%), where $L(T)$ is the fiber length at temperature T, and L_0 is the initial length. Negative and positive values denote thermotropic contraction and elongation, respectively. The graphs present the results from the fourth cycle of the test. TPU, thermoplastic urethane.

spinning process involving two-step cross-linking (*20*, *21*) (Fig. 1C). The diacrylate-terminated viscous LC oligomers used as precursors were extruded from a 3D printer nozzle at elevated temperatures and solidified by photopolymerization. Consequently, the nematic and smectic fibers displayed molecular orientations parallel and perpendicular to the fiber axis, respectively.

In general, polymer chains in conventional polymer fibers, as well as LCE fibers, are oriented along the fiber axis during manufacturing. This orientation parallel to the fiber axis results in negative thermal expansion coefficients along this axis. Hence, typical fibers experience contraction upon heating (*1*, *2*). Conventional synthetic fibers, including those made of polyester, nylon 66, nylon 6, and thermoplastic urethane (TPU), experienced minimal contraction ($\varepsilon < 2\%$) with increasing temperature and recovered their initial lengths upon cooling (Fig. 1D and figs. S1 and S2). The nematic fibers produced through the melt spinning displayed larger and reversible contracting actuation ($\varepsilon \approx 40\%$) upon heating (Fig. 1E). In contrast, the smectic fibers displayed molecular orientations perpendicular to the fiber axis, resulting in opposite actuation behavior compared to typical fibers, namely thermotropic elongation upon heating (Fig. 1F). The spontaneous thermotropic elongation of our smectic fibers, which exhibited a considerable and reversible actuation strain (~30%) with no need for additional structuring, such as heterochiral coiling (*2*, *38*), is remarkable.

Synthesis and rheological behavior of LCE fiber precursors

To produce both nematic and smectic LCE fibers, we first synthesized main-chain LC oligomers as LCE precursors. Step-growth polymerization was used to create LC oligomers using either a diacrylate-functionalized nematogen (RM82) or smectogen (C6BAPE) (Fig. 2A and fig. S3). The diacrylates were reacted with a chain extender (*n*-butylamine) at 65°C for 24 hours to induce aza-Michael addition (*30*). The molecular weights of the nematogenic and smectogenic oligomers were determined as 3800 and 4900 Da, respectively, using ^{1}H nuclear magnetic resonance (NMR) spectroscopy and size exclusion chromatography (SEC) (figs. S4 to S6), and the oligomer phase behavior was probed using polarized optical microscopy (POM) and differential scanning calorimetry (DSC). Upon cooling from the isotropic phase, schlieren and fan-shaped textures were observed by POM for the nematogenic and smectogenic oligomers, respectively, indicating the formation of characteristic mesophases (Fig. 2B and fig. S7). The second-heating DSC thermograms of the LC oligomers revealed the occurrence of a glass transition (T_g) and isotropization (T_i) (Fig. 2C and Table 1). The T_i for the nematogenic oligomer (97°C) was 55°C higher than that of the smectogenic oligomer, which was attributed to weaker π-π interactions between the mesogenic segments of C6BAPE (*46*). In addition, the smectogenic oligomer exhibited a more pronounced endothermic peak and larger enthalpy ($\Delta H \approx 8.3$ J g^{-1}) than its nematogenic counterpart ($\Delta H \approx 1.8$ J g^{-1}), which indicated that a greater amount of energy was required to disrupt the smectic ordering.

The rheological properties of LC oligomers can provide insights for achieving proper alignment during extrusion (*47*–*50*). The steady-shear viscosities of nematogenic and smectogenic oligomers at various temperatures and shear rates are presented in Fig. 2 (D and E), respectively. The data obtained for the nematogenic oligomer indicated the presence of two distinct regimes, namely Newtonian behavior at low shear rates (0.001 to 10 s^{-1}) and shear thinning [attributed to the flow alignment of mesogens (*47*)] at high shear rates (10 to 100 s^{-1}). Compared with its nematogenic counterpart, the smectogenic oligomer exhibited a 10 to 100 times higher viscosity because of the greater ordering in the smectic phase. Three shear viscosity regimes were identified for the smectic oligomer, especially below T_i, namely Newtonian behavior at low shear rates (0.001 to 0.03 s^{-1}), first thinning at intermediate shear rates (0.03 to 10 s^{-1}), and second thinning at high shear rates (10 to 100 s^{-1}). The first thinning was attributed to the alignment of smectic domains with layers oriented parallel to the flow direction, while the second thinning was ascribed to the alignment of oligomeric mesogens along the flow direction at sufficiently high shear rates (*48*, *49*). In the case of the isotropic melt ($T > 45$°C), only one shear thinning was observed at very high shear rates (>50 s^{-1}).

To validate the LC oligomer alignment proposed based on the results of rheological measurements, we prepared shear-aligned LCE films by blade coating (Fig. 2F and fig. S8) different oligomers at various speeds (5 to 100 mm s^{-1}) and elevated temperatures (60° and 40°C for nematogenic and smectogenic oligomers, respectively). Photopolymerization was used to fix the alignment. These films were subsequently heated above T_i, and their dimensional changes were monitored to shed light on the behavior of LC oligomers during shear alignment, as the thermotropic actuation of LCE films is determined by their molecular orientation. On the one hand, nematic LCE films underwent thermotropic contraction (42 to 45%) when heated to 140°C, which suggested a director alignment parallel to the shear flow regardless of the coating speed (Fig. 2, G and H, and figs. S9 and S10). On the other hand, the thermotropic actuation of the smectic LCE films was strongly dependent on the coating speed, with thermotropic elongation (~15%) and contraction (14 to 22%) observed at low (5, 10, and 20 mm s^{-1}) and high (50 and 100 mm s^{-1}) coating speeds, respectively (Fig. 2, G and H, and figs. S11 and S12). These results suggested that the director alignment of smectic LCE films switched from perpendicular to parallel to the shear direction at sufficiently high coating speeds (i.e., high shear rates), which agreed well with the results of the rheological property measurements.

Production, microstructure, and thermotropic actuation of LCE fibers

After characterizing the LC oligomers, we subjected them to melt spinning at various temperatures to produce three types of LCE fibers, namely nematic fibers extruded from the nematic phase (50°C), smectic fibers extruded from the smectic phase (40°C), and smectic fibers extruded from the isotropic phase (50°C). The unique flow behaviors of the oligomeric mesophases during extrusion led to distinct molecular orientations (i.e., director orientation parallel or perpendicular to the long axis) (Fig. 3, A to C). The extruded oligomers were exposed to ultraviolet (UV) light near the nozzle to achieve sufficient strength for transfer to the rotating mandrel (fig. S13 and movie S1). During collection, the partially cured fibers underwent a second UV curing to complete cross-linking, resulting in a high gel fraction (fig. S14). The resultant nematic, smectic, and iso-spun smectic fibers featured a round shape with uniform diameters of 430, 480, and 380 μm, respectively, as determined by scanning electron microscopy (SEM) (fig. S15).

The microstructure and orientation of the LCE fibers were investigated using wide-angle x-ray scattering (WAXS) analysis, with the lateral fiber surface exposed to the beam (Fig. 3, D to F, and fig. S16). The nematic fibers exhibited two wide-angle scatterings on the meridian, indicating a weak lateral ordering between mesogens, and

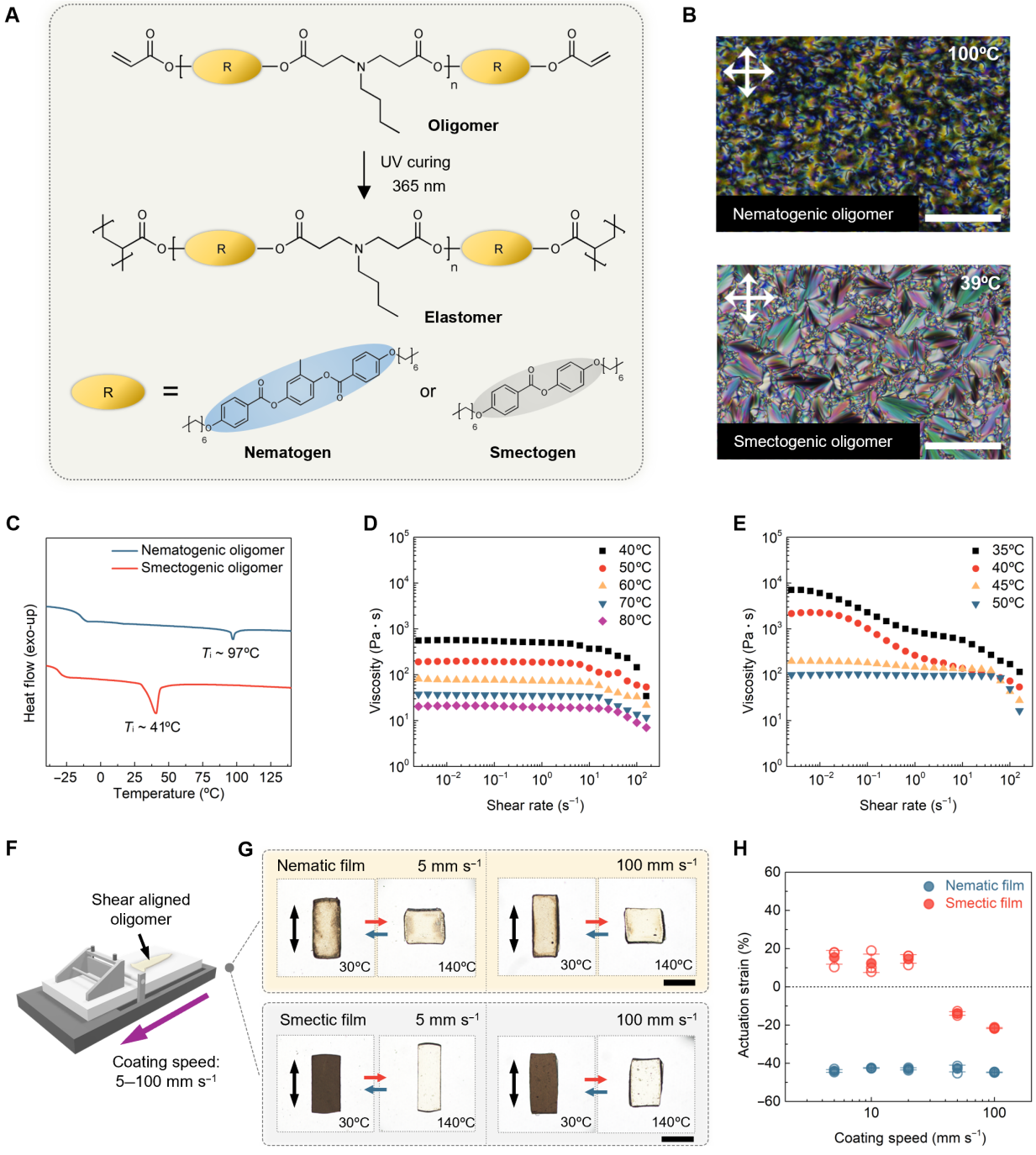

Fig. 2. Reaction scheme and phase/rheological behavior of LC oligomers and actuation of shear-aligned LCE films. (**A**) Reaction scheme of LC oligomers and LC elastomers incorporating the nematogen and smectogen. (**B**) POM images of the LC oligomers in nematic (top) and smectic (bottom) phases. Scale bars, 200 μm. (**C**) Second-heating DSC curves of the LC oligomers. (**D** and **E**) Shear viscosity as a function of the shear rate at various temperatures for (D) nematogenic and (E) smectogenic oligomers. (**F**) Schematic showing the shear alignment of LC oligomers blade-coated at different speeds. (**G**) Thermotropic actuation of shear-aligned nematic (top) and smectic (bottom) films prepared at different coating speeds. Scale bars, 500 μm. Double arrows indicate the coating direction. (**H**) Actuation strain along the long axis of nematic and smectic films prepared at various coating speeds, with hollow circles representing individual data points, solid circles indicating means, and error bars showing SDs. $N = 3$.

Table 1. Properties of LCE fibers.

Material	Phase transition*		ΔH (J g^{-1})*	Extrusion temp.† (°C)	M_n‡ (kDa)	M_n§ (kDa)	M_w§ (kDa)	Đ§	Mechanical properties¶			Actuation strain#,** (%)
	T_g (°C)	T_i (°C)							Tensile strength (MPa)	Strain (%)	Elastic modulus (MPa)	
Nematogenic oligomer	−16	99	1.8	–	3.8	2.2	7.1	3.3	–	–	–	–
Smectogenic oligomer	−30	42	8.3	–	4.9	3.4	10.7	3.2	–	–	–	–
Nematic fiber	−7	113	1.0	50	–	–	–	–	11.7 ± 0.7	187.7 ± 10.0	9.4 ± 1.1	−48.6 ± 1.0#
Smectic fiber	−20	52	5.3	40	–	–	–	–	4.5 ± 0.7	455.4 ± 77.7	4.0 ± 0.2	+30.8 ± 1.4#
Smectic fiber (iso-spun)	−21	48	4.8	50	–	–	–	–	11.4 ± 3.1	182.7 ± 36.0	12.4 ± 0.8	−23.2 ± 5.3#
Reinforced nematic fiber	−4	114	0.9	40	–	–	–	–	18.5 ± 0.6	112.2 ± 5.3	16.1 ± 0.5	−44**
Reinforced smectic fiber	−17	49	1.9	30	–	–	–	–	12.5 ± 0.1	269.8 ± 11.2	3.5 ± 0.1	+34**

*Determined from the second-heating DSC curves at a rate of 10°C min^{-1} under nitrogen. †Extruder barrel and nozzle temperature during LCE fiber production. ‡Determined by ^{1}H NMR end-group analysis. §Determined by SEC. ¶Determined by tensile testing using dynamic mechanical analysis at 25°C. #Determined using an optical microscope during heating and cooling. **Determined by dynamic mechanical analysis in the isostress mode. Actuation strain (%) $= \left|L(T) - L_0\right| / L_0 \times 100$ (%), where $L(T)$ and L_0 are the fiber length at temperature T and initial length, respectively. (−) and (+) indicate thermotropic contraction and elongation, respectively.

four small-angle spots on the equator, attributed to the cybotactic nematic phase (Fig. 3D and fig. S17) (*51*). This result suggested that the mesogens in the nematic fibers were aligned along the fiber axis. The smectic fibers displayed wide-angle scatterings on the equator and sharp small-angle reflections on the meridian, which indicated the presence of the smectic A phase. The 2D WAXS patterns of the smectic fibers suggested that the layers and mesogens were aligned parallel and perpendicular to the fiber axis, respectively (Fig. 3E and fig. S18). The extraordinary molecular orientation in the smectic fibers originated from the shear flow of the smectic melt, which aligned the smectic layers along the flow direction (*43*). The 2D WAXS pattern of the iso-spun smectic fibers showed wide-angle scatterings on the meridian and sharp small-angle reflections on the equator, resembling that of the smectic fibers except for a 90° rotation, which suggested that the layers and mesogens in the former fibers were aligned perpendicular and parallel to the fiber axis, respectively (Fig. 3F and fig. S19). Although the oligomer was extruded from the isotropic phase, UV curing was performed at room temperature (i.e., in the smectic phase), resulting in the iso-spun LCE fibers regaining smectic A order. However, the mesogens remained oriented parallel to the fiber axis because of the shear flow experienced in the isotropic phase. We further evaluated the fiber orientation parameter (S) based on the azimuthal scan profiles of wide-angle scattering at $q_w \approx 1.4$ Å (figs. S17 to S19). The values obtained for the nematic, smectic, and iso-spun smectic fibers (0.37, 0.20, and 0.42, respectively) were comparable with those observed for LCEs with rheological alignment (*4*).

The spontaneous and reversible shape morphing of uniformly aligned LCEs is driven by the LC order-disorder transition (*5*). Consequently, the operating temperature of LCE actuators is strongly affected by this thermal transition. The T_i values of the nematic, smectic, and iso-spun smectic fibers equaled 113°, 52°, and 48°C, respectively, as determined from the corresponding second-heating DSC curves (fig. S20). The T_i of the iso-spun smectic fibers was slightly lower than that of the smectic fibers, despite both fibers originating from the same LC oligomer, which was attributed to the extrusion of the former fibers from the isotropic phase (*52*).

To study the thermotropic actuation of our LCE fibers, we monitored their dimensional changes during temperature-controlled optical microscopy analysis (Fig. 3, G and H, and movie S2). When heated above T_i, the nematic fibers exhibited thermotropic contraction (49%), whereas the smectic and iso-spun smectic fibers underwent spontaneous elongation (31%) and contraction (23%), respectively. The contradicting thermal actuation behaviors of LCEs derived from a single precursor were attributed to differences in the mesogen orientations relative to the fiber axis. Upon cooling below T_i, all fibers exhibited reversible actuation, returning to their initial lengths. Figure 3I displays the effects of temperature on the S values of the fibers. Upon heating above T_i, the S values of all fibers approached zero, which indicated a loss of LC ordering and suggested that the thermal actuation was due to the LC order-disorder transition. Controlled nematic and smectic fibers produced from another nematogen (RM257) and smectogen (C11M) behaved similarly to RM82-based nematic fibers and C6BAPE-based smectic fibers (*53*), which suggested that extrusion from the smectic phase was the key for achieving spontaneous thermotropic elongation (figs. S21 to S24).

Mechanical property reinforcement and active textile demonstration

The mechanical properties of LCE fibers are strongly influenced by their molecular orientation and are crucial for textile manufacturing. When uniaxially stretched, all LCE monofilaments displayed deformability (strain = 183 to 455%) with nonlinear stress-strain responses (Fig. 4A). The nematic and iso-spun smectic fibers exhibited comparable mechanical properties, featuring tensile strengths of 11.4 to 11.7 MPa, elastic moduli of 9.4 to 12.4 MPa, and strains at break of 183 to 188%. In contrast, the smectic fibers showed softer

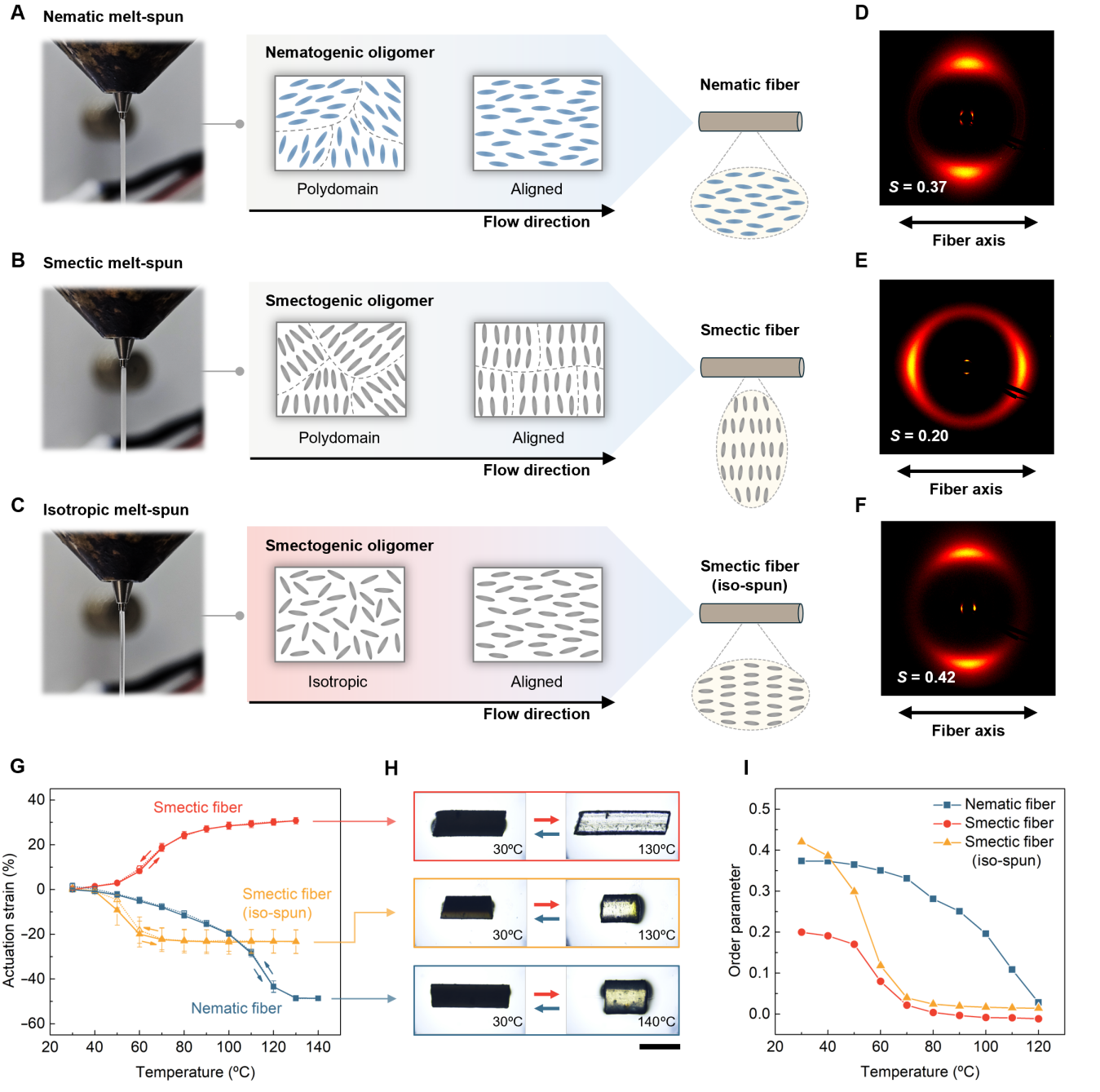

Fig. 3. Melt-spun LCE fibers: Molecular alignment and thermal actuation. (**A** to **C**) Photographs of oligomeric filaments at the nozzle exit. The nematic and smectic filaments are opaque, whereas isotropic filaments are transparent. Schematic of molecular alignment during the extrusion of LC oligomers from (A) nematic, (B) smectic, and (C) isotropic phases. (**D** to **F**) Molecular alignments and corresponding 2D wide-angle x-ray scattering (WAXS) patterns of (D) nematic, (E) smectic, and (F) iso-spun smectic fibers, with fiber axes aligned horizontally. *S* values represent the order parameter. (**G**) Thermal actuation strains of LCE fibers. (**H**) Corresponding optical microscopy images. Scale bar, 500 μm. Actuation strain (%) = $[L(T) - L_0] / L_0 \times 100$ (%), where $L(T)$ is the fiber length at temperature T, and L_0 is the initial length. Negative and positive values denote thermotropic contraction and elongation, respectively. (**I**) Order parameter of the LCE fibers as a function of the temperature.

features, e.g., a tensile strength of 4.5 MPa, an elastic modulus of 4.0 MPa, and a strain at break of 455%. In addition, the soft elastic plateau of these fibers was considerably extended compared with those of their nematic and iso-spun smectic counterparts. The considerable compliance and extended soft elastic plateau of the smectic fibers were attributed to the perpendicular orientation of the mesogens to the fiber axis, which enabled a greater degree of mesogenic reorientation during elongation.

To apply our LCE fibers to textile manufacturing, it was necessary to enhance their mechanical properties. In particular, the overly soft elastic response of the smectic fibers was undesirable. To address this limitation, we introduced a small amount (2.5 wt %)

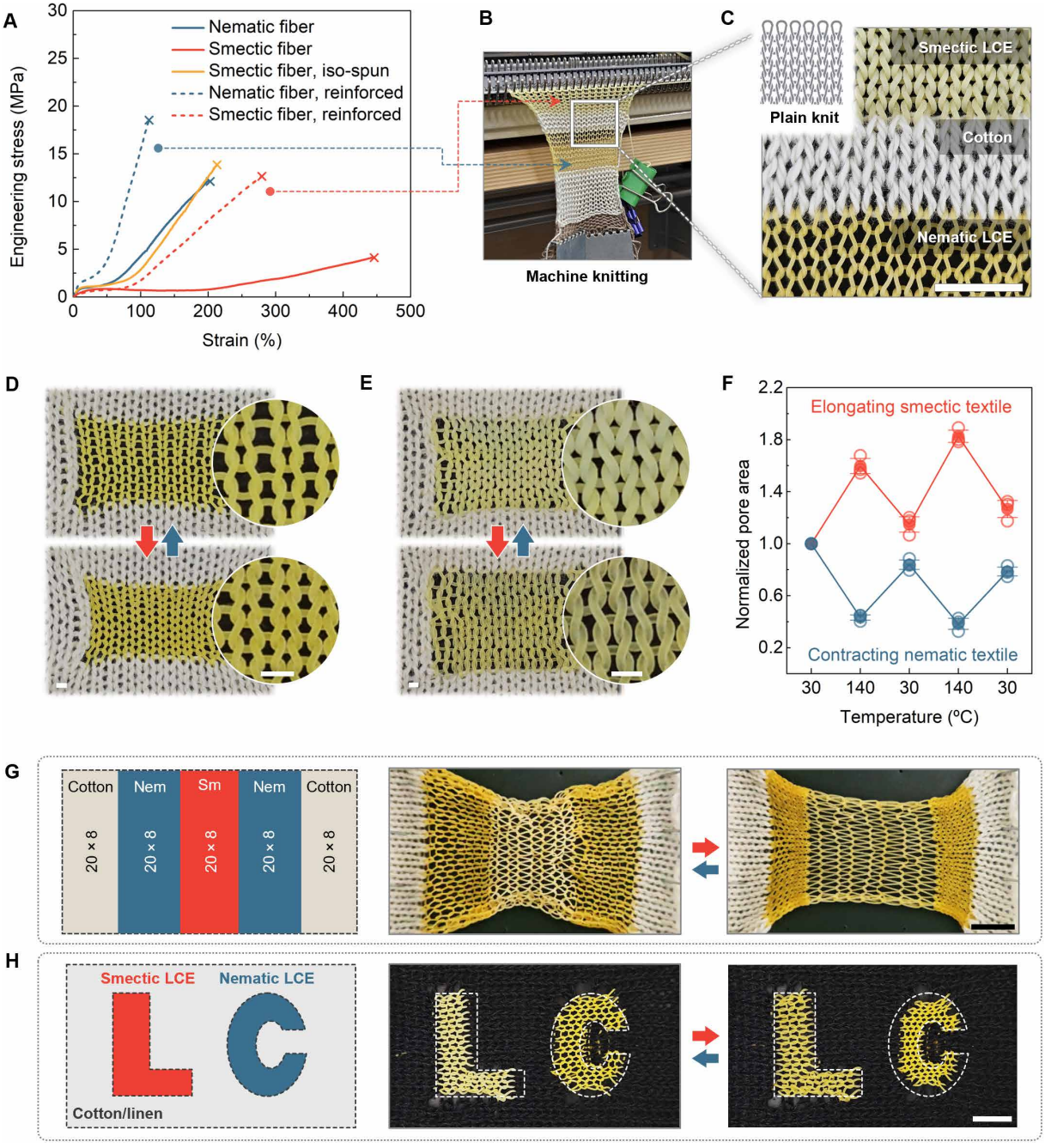

Fig. 4. Mechanical properties, actuation, and active textile demonstration. (**A**) Stress-strain responses of LCE fibers. The experiment was repeated three times for each sample, yielding similar results. (**B**) Fabrication of LCE textiles using machine knitting. (**C**) A photograph of the plain knitted LCE textile. Scale bar, 1 cm. (**D**) Actuation of an active textile knitted using nematic (yellow) and cotton (white) fibers showing a decrease in the pore area upon heating. Scale bar, 2 mm. (**E**) Actuation of an active textile knitted using smectic (yellow) and cotton (white) fibers showing an increase in the pore area upon heating. Scale bar, 2 mm. (**F**) Change in the normalized pore area of nematic and smectic fiber–based active textiles during cyclic heating and cooling. (**G**) Design (left) and spatially distinct thermal actuation (right) of a hybrid textile showing a decrease and increase in the pore area in regions with nematic and smectic fibers, respectively. Numbers represent the course (*20*) and wale (*8*) of the plain knit. Scale bar, 1 cm. (**H**) Design (left) and spatially distinct thermal actuation (right) of an active textile patterned with the letters "LC." The dashed outlines in "L" and "C" are included for ease of comparison before and after actuation. Scale bar, 1 cm.

of a triallyl cross-linker into the LC oligomer mixture before melt spinning (fig. S25). This modification markedly increased the tensile strength of the fiber and reduced the soft elastic response while preserving the unique mesogen orientation (Fig. 4A and figs. S26 and S27). The thermal actuation of the reinforced fibers was investigated by monitoring the length changes under a constant load (10^{-4} N). Cyclic heating and cooling were performed, with the actuation strain in the fourth cycle presented in Fig. 1 (E and F). The nematic and smectic fibers exhibited fully reversible thermotropic actuation, experiencing contraction/elongation ($\varepsilon \approx 40\%$) and elongation/contraction ($\varepsilon \approx 30\%$) upon heating/cooling, respectively (fig. S28). These results suggested that the actuation performance of both reinforced fibers did not notably degrade after additional cross-linking.

The ability to switch the actuation direction of LCE fibers provides opportunities for diverse applications. As a proof of concept, we fabricated active LCE textiles from nematic and smectic fibers using machine knitting (Fig. 4, B and C, and movie S3). Upon heating above T_i, the interlocking loops in these textiles underwent substantial dimensional changes that resulted in pore size variation, with the nematic textile experiencing a 55% decrease and smectic textile exhibiting a 57% increase (Fig. 4, D to F; fig. S29; and movies S4 and S5). These results demonstrate the feasibility of creating active textiles capable of increasing body comfort by adjusting breathability in response to temperature variations. Textiles knitted from smectic fibers can easily realize this function by experiencing a pore size increase upon heating, which is not achievable using conventional or LCE fibers. The variation in the pore size can be tailored by adjusting the interval between fibers during knitting or modifying the mechanical properties of the fiber. Last, we prepared active textiles by hybridizing nematic and smectic fibers, achieving spatially distinct actuation modes (Fig. 4, G and H, and movies S6 and S7).

DISCUSSION

Smectic LCE-based actuating fibers undergoing considerable spontaneous elongation when heated above their isotropization temperature were prepared. This elongation originated from the orthogonal orientation of smectogenic mesogens relative to the fiber axis. The mesogen alignment was exclusively dictated by the type of the LC phase present during extrusion, with nematic- or isotropic-phase extrusion leading to contracting fibers and smectic-phase extrusion resulting in elongating fibers. This simple approach enabled the fabrication of actuating fibers exhibiting two distinct actuation modes from the same LCE precursor. Active textiles were prepared from contracting nematic fibers, elongating smectic fibers, and their hybrids, experiencing pore size changes in response to temperature variations. The ability to steer the actuation direction of LCE fibers may enable the advancement of intelligent textiles, artificial muscles, and soft robots.

MATERIALS AND METHODS

Materials

1,4-Bis[4-(6-acryloyloxyhexyloxy)benzoyloxy]-2-methylbenzene (RM82) and 1,4-bis[4-(3-acryloyloxypropyloxy)benzoyloxy]-2-methylbenzene (RM257) were purchased from Wilshire. 4-(6-(Acryloyloxy)hexyloxy)phenyl 4-(6-(acryloyloxy)hexyloxy)benzoate (C6BAPE) and 1,4-bis[4-(11-acryloyloxyundecyloxy)benzoyloxy]-2-methylbenzene (C11M) were purchased from Synthon Chemical. *n*-Butylamine and 1,3,5-triallyl-1,3,5-triazine-2,4,6(1*H*,3*H*,5*H*)-trione (TATATO) were purchased from Sigma-Aldrich. The photoinitiator (Irgacure 369) was donated by BASF Corporation. All materials were used as received. Polyester and thermoplastic polyurethane fibers were donated by Sambu Fine Chemical. Nylon 6 and nylon 66 fibers were purchased from CFX.

Synthesis of LC oligomers

LC oligomers were synthesized via aza-Michael addition-based step-growth polymerization from diacrylate-functionalized mesogenic monomers (RM82, C6BAPE, RM257, or C11M) and *n*-butylamine (1.1:1, mol/mol) in the presence of I-369 (2.5 wt %). For the reinforced fiber precursors, the molar ratio was adjusted to 1.15:1, with the TATATO and I-369 loadings equaling 2.5 wt % each. Thorough mixing was conducted by vortexing upon heating, following which the mixtures were placed in a convection oven at 65°C for 24 hours to induce oligomerization.

Preparation of LCE films

The LC oligomers were blade-coated using an automatic film coater (MSK-AFA-III, MTI Corporation) and a poly(ethylene terephthalate) sheet as a substrate. The gap between the doctor blade and substrate was set to 100 μm. Nematogenic and smectogenic oligomers were coated at 60° and 40°C, respectively, using coating speeds of 5, 10, 20, 50, and 100 mm s^{-1}, and subjected to UV cross-linking (OmniCure S1500, $\lambda = 365$ nm, 70 mW cm^{-2}) for 30 min to obtain aligned LCE films.

Production of LCE fibers

The LCE fibers were produced using a 3D printer (Dr. INVIVO 4D, Rokit Healthcare) equipped with a pneumatic extruder and a 0.6-mm-diameter nozzle. A rotating mandrel (BLDC motor 30W, DISSOL) wrapped with a Teflon sheet was used to pull and collect the fibers. Two UV curing devices positioned near the nozzle (OmniCure S1500, $\lambda = 365$ nm, 70 mW cm^{-2}) and mandrel (OmniCure S1500, $\lambda = 320$ to 500 nm, 70 mW cm^{-2}) were used to photocross-link the oligomeric filaments at different stages of the extrusion process (fig. S13). The LC oligomers were extruded through the nozzle at a constant pressure of 500 kPa and a temperature of 50°, 40°, 50°, 60°, or 50°C to produce nematic, smectic, iso-spun smectic, RM257-derived, or C11M-derived fibers, respectively. The reinforced nematic and smectic fibers were extruded at 40° and 30°C, respectively. The extruded LC oligomers were partially cross-linked by the first UV curing device near the nozzle to provide sufficient mechanical strength for transfer to the rotating mandrel. Subsequently, the filaments were subjected to the second UV curing (30 min) while being pulled and collected onto the rotating mandrel. The mandrel rotation speed was adjusted by controlling the oligomer flow rate.

Characterization

^{1}H NMR spectra were recorded on an Agilent ProPulse 600 MHz spectrometer in $CDCl_3$ as the solvent. SEC analysis was performed on an Agilent 1260 Infinity II instrument equipped with a G7110B isocratic pump and G7114A refractive index detector at a temperature of 40°C and a flow rate of 1 ml min^{-1}. Polystyrene standards were used to construct a calibration curve. POM images were obtained using a Nikon Eclipse LV100N POL optical microscope equipped with a

heating stage (Linkam LTS420). This setup was used to characterize the texture and phase behavior of LC oligomers as well as the alignment and thermotropic actuation of LCEs. The textures of the LC oligomers were identified using a glass cell. Two glass slides were washed with an Alconox solution, acetone, and isopropanol, treated with O_2 plasma (Harrick PDC-001), spin-coated with a poly(vinyl alcohol) solution (1 wt % in deionized water) at 2300 rpm for 30 s, and assembled using a 15-μm spacer. The resulting cell was filled with the photoinitiator-free LC mixture through capillary action, oligomerized at 65°C for 24 hours, and subjected to POM analysis. DSC measurements (TA Instruments, Discovery DSC 25) were conducted between −50° and 150°C at a rate of 10°C min^{-1} under nitrogen. The steady-shear viscosities of the LC oligomers were measured using a rotational rheometer (TA Instruments, HR-20) with a 25-mm parallel plate geometry and a 600- to 1050-μm gap. In these experiments, the samples were placed on a Peltier plate, and their viscosities were measured under rotational shear between the parallel plates and Peltier plate at various temperatures. During these measurements, the shear rate was increased from 0.001 to 100 s^{-1}. The SEM images of the LCE fibers were obtained using a GEMINI 500 field emission scanning electron microscope at an acceleration voltage of 10 kV. Fiber cross sections were prepared by fracturing after freezing in liquid nitrogen. Each sample was sputter-coated with a 3-nm layer of platinum. The stress-strain responses of the fiber samples (7 mm in length) were measured at room temperature using a dynamic mechanical analyzer (TA Instruments, RSA-G2) equipped with a tension film clamp at a strain rate of 100% min^{-1}. Cyclic thermotropic actuations were characterized using a dynamic mechanical analyzer (TA Instruments, DMA Q850) with a tension film clamp in the isostress mode. Nematic fibers (10 mm in length) were subjected to repeated heating and cooling between 20° and 140°C at a rate of 3°C min^{-1} under a preload of 10^{-4} N, while smectic fibers were cycled between 10° and 130°C because of their lower actuation temperature.

WAXS analysis

WAXS patterns were recorded using synchrotron radiation with λ = 1.119 Å (E = 11.08 keV) at the 9A U-SAXS beamline of the Pohang Accelerator Laboratory, Republic of Korea. 2D scattering patterns were acquired using a 2D charge-coupled device area detector (Rayonix MX170-HS) at a sample-to-detector distance of 0.21 m. 1D intensity-scattering vector [$\mathbf{q} = (4\pi/\lambda)\sin(\theta/2)$, where θ is the scattering angle] profiles were derived from the 2D patterns. Temperature-resolved WAXS measurements were carried out using a custom-made sample holder equipped with a heating apparatus. The S values were calculated from azimuthal plots using the following equation (*54*)

$$S = \langle P_2 \rangle = 1 - N^{-1}\frac{3}{2}\int_0^{\frac{\pi}{2}} I(\phi)\left[\sin^2\phi + \left(\sin\phi\cos^2\phi\right)\ln\frac{1+\sin\phi}{\cos\phi}\right]d\phi$$

where $N = \int_0^{\frac{\pi}{2}} I(\phi)d\phi$, ϕ is the azimuthal angle, and $I(\phi)$ is the azimuthal angle-dependent intensity at a constant scattering vector $\mathbf{q}$.

Fabrication and thermal actuation of LCE textiles

The LCE textiles were knitted in plain patterns using a Brother KH881 knitting machine. Before knitting, the LCE fibers were lightly coated with corn starch to eliminate surface stickiness. During knitting, the fiber tension was adjusted on a scale of 1 to 10 using a tension dial. For example, the white cotton yarn and black cotton/linen yarn presented in Fig. 4 were knitted with the tension set to 3 and 6, respectively, while the LCE fibers were knitted with the tension set to 6. For thermal actuation analyses, the LCE textiles were placed on a heating stage, and shape changes were monitored at various temperatures using a smartphone camera. Pore area and size variations were analyzed by examining video frames using ImageJ software. The pore area was normalized by calculating the ratio of pixels representing the pore area at a specific temperature (T) to the pixels representing the initial pore area.

Supplementary Materials

The PDF file includes:
Supplementary Text
Figs. S1 to S29
Legends for movies S1 to S7

Other Supplementary Material for this manuscript includes the following:
Movies S1 to S7

REFERENCES AND NOTES

1. V. B. Gupta, J. Radhakrishnan, S. K. Sett, Interaction between thermal shrinkage and crystallization in axially oriented poly(ethylene terephthalate) fibers and films. *Polymer* **34**, 3814–3822 (1993).
2. C. S. Haines, M. D. Lima, N. Li, G. M. Spinks, J. Foroughi, J. D. W. Madden, S. H. Kim, S. Fang, M. J. de Andrade, F. Göktepe, Ö. Göktepe, S. M. Mirvakili, S. Naficy, X. Lepró, J. Oh, M. E. Kozlov, S. J. Kim, X. Xu, B. J. Swedlove, G. G. Wallace, R. H. Baughman, Artificial muscles from fishing line and sewing thread. *Science* **343**, 868–872 (2014).
3. Z. Zhu, J. Di, X. Liu, J. Qin, P. Cheng, Coiled polymer fibers for artificial muscle and more applications. *Matter* **5**, 1092–1103 (2022).
4. K. M. Herbert, H. E. Fowler, J. M. McCracken, K. R. Schlafmann, J. A. Koch, T. J. White, Synthesis and alignment of liquid crystalline elastomers. *Nat. Rev. Mater.* **7**, 23–38 (2022).
5. M. Warner, E. M. Terentjev, *Liquid Crystal Elastomers* (Oxford Univ. Press, 2007).
6. H.-H. Yoon, D.-Y. Kim, K.-U. Jeong, S.-K. Ahn, Surface aligned main-chain liquid crystalline elastomers: Tailored properties by the choice of amine chain extenders. *Macromolecules* **51**, 1141–1149 (2018).
7. K. Kim, Y. Guo, J. Bae, S. Choi, H. Y. Song, S. Park, K. Hyun, S.-K. Ahn, 4D printing of hygroscopic liquid crystal elastomer actuators. *Small* **17**, 2100910 (2021).
8. P. E. S. Silva, X. Lin, M. Vaara, M. Mohan, J. Vapaavuori, E. M. Terentjev, Active textile fabrics from weaving liquid crystalline elastomer filaments. *Adv. Mater.* **35**, 2210689 (2023).
9. J. Sun, W. Liao, Z. Yang, Additive manufacturing of liquid crystal elastomer actuators based on knitting technology. *Adv. Mater.* **35**, 2302706 (2023).
10. X. Wang, H. Shao, J. Tang, J. Chen, Y. Huang, J. Pan, Y. Zhang, W. Wang, J. Jiang, N. Chen, Braided liquid crystal elastomer fiber actuator with programmable deformation for artificial muscles. *Adv. Mater. Technol.* **8**, 2300814 (2023).
11. J. Naciri, A. Srinivasan, H. Jeon, N. Nikolov, P. Keller, B. R. Ratna, Nematic elastomer fiber actuator. *Macromolecules* **36**, 8499–8505 (2003).
12. S. Nocentini, D. Martella, D. S. Wiersma, C. Parmeggiani, Beam steering by liquid crystal elastomer fibers. *Soft Matter* **13**, 8590–8596 (2017).
13. L. Liu, M. del Pozo, F. Mohseninejad, M. G. Debije, D. J. Broer, A. P. H. J. Schenning, Light tracking and light guiding fiber arrays by adjusting the location of photoresponsive azobenzene in liquid crystal networks. *Adv. Opt. Mater.* **8**, 2000732 (2020).
14. D. S. Kim, Y.-J. Lee, Y. Wang, J. Park, K. I. Winey, S. Yang, Self-folding liquid crystal network filaments patterned with vertically aligned mesogens. *ACS Appl. Mater. Interfaces* **14**, 50171–50179 (2022).
15. Y. Geng, J. P. F. Lagerwall, Multiresponsive cylindrically symmetric cholesteric liquid crystal elastomer fibers templated by tubular confinement. *Adv. Sci.* **10**, 2301414 (2023).
16. L. Zhao, H. Tian, H. Liu, W. Zhang, F. Zhao, X. Song, J. Shao, Bio-inspired soft-rigid hybrid smart artificial muscle based on liquid crystal elastomer and helical metal wire. *Small* **19**, 2206342 (2023).
17. E.-K. Fleischmann, F. R. Forst, R. Zentel, Liquid-crystalline elastomer fibers prepared in a microfluidic device. *Macromol. Chem. Phys.* **215**, 1004–1011 (2014).
18. N. Najiya, N. Popov, V. S. R. Jampani, J. P. F. Lagerwall, Continuous flow microfluidic production of arbitrarily long tubular liquid crystal elastomer peristaltic pump actuators. *Small* **19**, 2204693 (2023).
19. S. V. Ahir, A. R. Tajbakhsh, E. M. Terentjev, Self-assembled shape-memory fibers of triblock liquid-crystal polymers. *Adv. Funct. Mater.* **16**, 556–560 (2006).

20. D. J. Roach, C. Yuan, X. Kuang, V. C.-F. Li, P. Blake, M. Lechuga Romero, I. Hammel, K. Yu, H. J. Qi, Long liquid crystal elastomer fibers with large reversible actuation strains for smart textiles and artificial muscles. *ACS Appl. Mater. Interfaces* **11**, 19514–19521 (2019).
21. X. Lin, M. O. Saed, E. M. Terentjev, Continuous spinning aligned liquid crystal elastomer fibers with a 3D printer setup. *Soft Matter* **17**, 5436–5443 (2021).
22. S. J. D. Lugger, T. A. P. Engels, R. Cardinaels, T. Bus, D. J. Mulder, A. P. H. J. Schenning, Melt-extruded thermoplastic liquid crystal elastomer rotating fiber actuators. *Adv. Funct. Mater.* **33**, 2306853 (2023).
23. C. Ohm, M. Morys, F. R. Forst, L. Braun, A. Eremin, C. Serra, R. Stannarius, R. Zentel, Preparation of actuating fibers of oriented main-chain liquid crystalline elastomers by a wetspinning process. *Soft Matter* **7**, 3730–3734 (2011).
24. J. Sun, Y. Wang, W. Liao, Z. Yang, Ultrafast, high-contractile electrothermal-driven liquid crystal elastomer fibers towards artificial muscles. *Small* **17**, 2103700 (2021).
25. D. Wu, Y. Zhang, H. Yang, A. Wei, Y. Zhang, A. Mensah, R. Yin, P. Lv, Q. Feng, Q. Wei, Scalable functionalized liquid crystal elastomer fiber soft actuators with multi-stimulus responses and photoelectric conversion. *Mater. Horiz.* **10**, 2587–2598 (2023).
26. X. Dong, X. Zhou, L. Li, X. Cao, J. Xu, S. Dai, Y. Jiang, Q. Li, N. Yuan, J. Ding, Monodomain liquid crystal elastomer bionic muscle fibers with excellent mechanical and actuation properties. *iScience* **26**, 106357 (2023).
27. S. Krause, R. Dersch, J. H. Wendorff, H. Finkelmann, Photocrosslinkable liquid crystal main-chain polymers: Thin films and electrospinning. *Macromol. Rapid Commun.* **28**, 2062–2068 (2007).
28. A. Sharma, J. P. F. Lagerwall, Electrospun composite liquid crystal elastomer fibers. *Materials* **11**, 393 (2018).
29. Q. He, Z. Wang, Y. Wang, Z. Wang, C. Li, R. Annapooranan, J. Zeng, R. Chen, S. Cai, Electrospun liquid crystal elastomer microfiber actuator. *Sci. Robot.* **6**, eabi9704 (2021).
30. T. H. Ware, M. E. McConney, J. J. Wie, V. P. Tondiglia, T. J. White, Voxelated liquid crystal elastomers. *Science* **347**, 982–984 (2015).
31. C. M. Yakacki, M. Saed, D. P. Nair, T. Gong, S. M. Reed, C. N. Bowman, Tailorable and programmable liquid-crystalline elastomers using a two-stage thiol–acrylate reaction. *RSC Adv.* **5**, 18997–19001 (2015).
32. I. H. Kim, S. Choi, J. Lee, J. Jung, J. Yeo, J. T. Kim, S. Ryu, S.-K. Ahn, J. Kang, P. Poulin, S. O. Kim, Human-muscle-inspired single fiber actuator with reversible percolation. *Nat. Nanotechnol.* **17**, 1198–1205 (2022).
33. Z. Wang, K. Li, Q. He, S. Cai, A light-powered ultralight tensegrity robot with high deformability and load capacity. *Adv. Mater.* **31**, 1806849 (2019).
34. D. S. Kim, Y.-J. Lee, Y. B. Kim, Y. Wang, S. Yang, Autonomous, untethered gait-like synchronization of lobed loops made from liquid crystal elastomer fibers via spontaneous snap-through. *Sci. Adv.* **9**, eadh5107 (2023).
35. J. Forman, O. K. Afsar, S. Nicita, R. H.-J. Lin, L. Yang, M. Hofmann, A. Kothakonda, Z. Gordon, C. Honnet, K. Dorsey, N. Gershenfeld, H. Ishii, FibeRobo: Fabricating 4D fiber interfaces by continuous drawing of temperature tunable liquid crystal elastomers. *UIST 23* **19**, 1–17 (2023).
36. Y. Geng, R. Kizhakidathazhath, J. P. F. Lagerwall, Robust cholesteric liquid crystal elastomer fibers for mechanochromic textiles. *Nat. Mater.* **21**, 1441–1447 (2022).
37. Y. Wang, J. Sun, W. Liao, Z. Yang, Liquid crystal elastomer twist fibers toward rotating microengines. *Adv. Mater.* **34**, 2107840 (2022).
38. X. Hu, J. Li, S. Li, G. Zhang, R. Wang, Z. Liu, M. Chen, W. He, K. Yu, W. Zhai, W. Zhao, A. Q. Khan, S. Fang, R. H. Baughman, X. Zhou, Z. Liu, Morphology modulation of artificial muscles by thermodynamic-twist coupling. *Natl. Sci. Rev.* **10**, nwac196 (2023).
39. Y. Peng, Y. Cui, Advanced textiles for personal thermal management and energy. *Joule* **4**, 724–742 (2020).
40. J. Hu, M. Irfan Iqbal, F. Sun, Wool can be cool: Water-actuating woolen knitwear for both hot and cold. *Adv. Funct. Mater.* **30**, 2005033 (2020).
41. A. Romo-Uribe, A. H. Windle, "Log-rolling" alignment in main-chain thermotropic liquid crystalline polymer melts under shear: An in-situ WAXS study. *Macromolecules* **29**, 6246–6255 (1996).
42. W. R. Krigbaum, J. Watanabe, Thermotropic homopolyesters: 5. Investigation of the smectic phase of polyesters based on *p,p′*-bibenzoic acid. *Polymer* **24**, 1299–1307 (1983).
43. M. Tokita, K. Osada, S. Kawauchi, J. Watanabe, Thermotropic liquid crystals of main-chain polyesters with a mesogenic 4,4′-biphenyldicarboxylate unit XII. Unusual molecular orientation in fibers drawn from smectic melt. *Polym. J.* **30**, 687–690 (1998).
44. M. Tokita, J. Watanabe, Several interesting fields exploited through understanding of polymeric effects on liquid crystals of main-chain polyesters. *Polym. J.* **38**, 611–638 (2006).
45. B. Struth, K. Hyun, E. Kats, T. Meins, M. Walther, M. Wilhelm, G. Grübel, Observation of new states of liquid crystal 8CB under nonlinear shear conditions as observed via a novel and unique rheology/small-angle x-ray scattering combination. *Langmuir* **27**, 2880–2887 (2011).
46. J. M. McCracken, B. R. Donovan, K. M. Lynch, T. J. White, Molecular engineering of mesogenic constituents within liquid crystalline elastomers to sharpen thermotropic actuation. *Adv. Funct. Mater.* **31**, 2100564 (2021).
47. G. E. Bauman, J. A. Koch, T. J. White, Rheology of liquid crystalline oligomers for 3-D printing of liquid crystalline elastomers. *Soft Matter* **18**, 3168–3176 (2022).
48. S. O. Ilyin, I. I. Konstantinov, Rheology of highly ordered smectic phases based on biphenyl derivatives. *J. Mol. Liq.* **363**, 119872 (2022).
49. C. Bailey, K. Fodor-Csorba, J. T. Gleeson, S. N. Sprunt, A. Jákli, Rheological properties of bent-core liquid crystals. *Soft Matter* **5**, 3618–3622 (2009).
50. P. T. Mather, A. Romo-Uribe, C. D. Han, S. S. Kim, Rheo-optical evidence of a flow-induced isotropic−nematic transition in a thermotropic liquid-crystalline polymer. *Macromolecules* **30**, 7977–7989 (1997).
51. N. P. Godman, B. A. Kowalski, A. D. Auguste, H. Koerner, T. J. White, Synthesis of elastomeric liquid crystalline polymer networks via chain transfer. *ACS Macro Lett.* **6**, 1290–1295 (2017).
52. T. S. Hebner, C. N. Bowman, T. J. White, Influence of orientational genesis on the actuation of monodomain liquid crystalline elastomers. *Macromolecules* **54**, 4023–4029 (2021).
53. Y. Guo, J. Lee, J. Son, S.-K. Ahn, J.-M. Y. Carrillo, B. G. Sumpter, Decoding liquid crystal oligomer phase transitions: Toward molecularly engineered shape changing materials. *Macromolecules* **52**, 6878–6888 (2019).
54. M. Deutsch, Orientational order determination in liquid crystals by x-ray diffraction. *Phys. Rev. A* **44**, 8264–8270 (1991).

Acknowledgments: We thank H. Lee (Studio IT-DA) for help with the preparation of the knitted textiles. WAXS measurements were performed at the 9A U-SAXS beamline of the Pohang Accelerator Laboratory, Republic of Korea. **Funding:** S.A. acknowledge financial support from the National Research Foundation of Korea (NRF) grants funded by the Ministry of Science and ICT (MSIT) of the Korean Government (RS-2023-00208130 and RS-2023-00221396). T.H.W. acknowledges financial support from the National Science Foundation under grant no. 2147830. **Author contributions:** J.-H.L., S.O., and S.A. designed the experiments. J.-H.L. and S.O. conducted the overall experiments. J.-H.L. postprocessed the data. I.J. assisted with the production of the LCE fibers and the acquisition of optical images. Y.J.L. assisted with the experiments involving POM and SEM analyses. M.C.K. performed the rheological measurement. K.H. supervised the rheological experiments. J.S.P. supervised the fiber and textile production. T.H.W. advised on the theoretical description and discussed the overall experiments. J.-H.L. and S.A. wrote the paper. S.A. supervised the research. **Competing interests:** The authors declare that they have no competing interests. **Data and materials availability:** All data needed to evaluate the conclusions in the paper are present in the paper and/or the Supplementary Materials.

Submitted 10 October 2024
Accepted 17 December 2024
Published 17 January 2025
10.1126/sciadv.adt7613